Deposition Characteristics of Particles with Different Diameters in an Impingement-Effusion Structure with a Double-Wall Blade

W. Zhang†, P. Zhang, and Y. D. Wang

Department of Aeroengine, Shenyang Aerospace University, Shenyang 110000, China

†*Corresponding Author Email: 20093094@sau.edu.cn*

ABSTRACT

Ingestion and deposition of fine particles on the surface of the coolant passage degrade the blade's cooling performance. This paper proposes a deposition model to investigate the complex deposition characteristics of fine particles during repeated collision, adhesion, rebound, and removal events in the small space inside a typical impingement-effusion structure with a double-wall blade. The results show that the particles rarely collide with the wall and escape directly from the film hole outlet when the particle diameters are smaller than 0.5 μm. Most particles with diameters of 0.5 to 1.0 μm are deposited after the first collision around the stagnation point in an area 0.35 times the pin-fin diameter. Some particles with diameters of 1.0 to 3.0 μm are deposited in the stagnation region, but most are deposited between the two pin fins and near the film hole after the second collision. Particles with diameters larger than 3.0 μm are mainly deposited on the region enclosed by the adjacent pin fins and film holes after multiple collisions, and the escape rate of particles is higher than 30%. The escape rates of particles with diameters of 0.5 to 1.0 μm and 1.0 to 3.0 μm have the same trends, exhibiting a decrease followed by an increase with the increasing particle diameter. The particles entering the impingement-effusion structure, especially those with diameters of 0.7 -0.8 μm and 1.4 -2.4 μm, are primarily deposited on the target surface, resulting in the cooling performance degradation of double-walled blade.

1. INTRODUCTION

The bulletin on the distribution of global atmospheric pollutants released by the World Meteorological Organization indicates that particulate pollutants have accumulated in the atmosphere except in the polar regions and some ocean areas (Forsyth, 2017). Particles can be ingested into the engines of aircraft that encounter sand and ash, threatening flight safety. Military aircraft perform all-weather regional combat missions, and sand and dust are ingested into the engine during takeoff or landing in sandstorms, causing turbine blade blockage (Yonezawa et al., 2021). Two of the four engines of an L100 military transport plane failed, and the performance of the other two deteriorated when the aircraft flew through ash clouds after the eruption of Mount St. Helens (Boulanger et al., 2016). A thorough understanding of the deposition mechanism of sand ash in turbine components is crucial for preventing thermal failure of turbine components.

Fine particles accumulate on the blade surface after long-term engine operations. Wammack et al. (2008) and Bons et al. (2008) found that the valley formed in the early stage was filled in the later stage during deposition experiments at a cascade inlet temperature of 1150 ℃ and Mach number of 0.31. These results indicate that the sediment morphology affects the deposition characteristics. Laycock and Fletcher (2015) observed that the deposition rate (η_d) increased and decreased with an increase in the deposition surface temperature. Subsequent studies showed that a rise in the wall temperature increased the deposition region (Bonilla et al., 2013). Ai and Fletcher (2012) observed less deposition in the area covered with the film ejected from cylindrical holes and more deposition in the midspan area without the film. Tian et al. (2021) found that small particles were primarily deposited on the blade surface, and large particles mainly blocked film holes. These studies indicate that the particle size diameter significantly influences the deposition characteristics of particles. Jiang et al. (2018) observed

Nomenclature			
A	surface area	n_1	number of particle collision times
b	rebounding particle	P	probability
c	surface grid cell	p	particle
c_p	specific heat capacity	r	average frequency of a particle
D	diameter of the pin fin	St	Stokes number
d	deposited particle	s	adhering particle
d_I	impingement hole diameter	T	temperature
d_p	diameter of the particle	t	total times
e	escaping particle	t_p	migration time of the particle
F_d	drag force	u	migration velocity
F_s	Saffman's lift force	Vcr	critical capture velocity
F_t	thermophoretic force	$V\tau c$	critical wall shear velocity
f	fluid	V_s	characteristic velocity of the system
h	heat transfer coefficient	j	number of particles colliding with the wall
I	particles injected into the chamber at the inlet	τ_p	particle response time
i	colliding particle	τ_s	system response time
L_s	characteristic length of the system/m	ρ	density
m	mass	λ	fluid thermal conductivity
n	number of particles	μ	dynamic viscosity of the fluid
Nu	laterally averaged Nusselt number	η	rate
n_p	quantity per unit grid area		

that most particles in the coolant were trapped in the cooling passage of the turbine blade due to complex vortices induced by the ribs (Wang et al., 2021). By thermal infrared analyses, it is found that the particle sedimentation inside the nozzle stator vane resulted in a non-uniform reduce in the cooling performance of the blade (Li et al., 2020; Zhang et al., 2022). The likely reason is the non-uniform sedimentation on the inner surface of the blade.

Since the cooling passage of turbine blades is very narrow, it is difficult to detect and remove fly ash particles, increasing the risk of blocking the cooling passage. Cowan et al. (2010) observed that the windward side of the pin fin in the cooling passage was more likely to deposit fine particles. Thus, adjusting the pin-fin configuration can reduce the likelihood of particle sedimentation on the wall. Wylie et al. (2017) determined that a higher coolant flow rate caused an increase in the particle deposition mass, decreasing the blade's cooling performance. Schneider et al. (2003) observed that an increase in the coolant flow caused particles to be transported to the blade film cooling hole, resulting in a blockage. Thus, the maintenance period of the gas turbine had to be shortened. Land et al. (2008) proposed the impingement-effusion cooling structure to reduce the blockage of fine particles in the coolant to the film hole through the resisting mechanism of ash sand in the impingement plate and the trapping mechanism of ash sand in the target plate. Bowen et al. (2019) discovered that the size of a cone formed by particle deposition in the impingement-effusion cooling structure increased with an increase in the temperature.

Numerical prediction is an important method to understand the deposition characteristics inside a blade

because these characteristics are difficult to visualize. Particles ingested into an engine have an ignorable influence on the flow of the fluid (Brun et al., 2012). The Lagrange method can be used to trace the migration locus of fine ash in the flow field. Deposition models have been used to determine whether sand ash are sediment when they reach the wall. Brach and Dunn (1992) proposed the concept of the critical capture velocity (Vcr). Particles adhered to the surface when the Vcr was exceeded the normal collision velocity. Otherwise, they bounced off the surface after the collision. Subsequently, Soltani and Ahmadi (1994) and Das et al. (1995) showed that particles were deposited on the wall if the adhesion force of the particles exceeded the aerodynamic force of the fluid. Otherwise, the particles were removed from the surface. El-Batsh and Haselbacher (2002) derived an expression of the critical wall shear velocity (Vτc). Another threshold method for determining particle deposition is the critical viscosity model developed by Sreedharan and Tafti (2010). The model predicts the deposition probability based on the temperature of the impinging sand ash. The OSU deposition model proposed by Bons et al. (2017) predicted whether particles would adhere based on the deformation, adhesion, and shearing force caused by surrounding flows.

The proposed deposition model solves the influence of sedimentary surface properties on deposition in this paper. The properties of sedimentary surface were determined by the wall in the early stage of deposition and were determined by particles in the middle and late stages of deposition, so the model can accurately analyze the deposition mechanism and characteristics of particles in a small space inside the impingement-effusion structure of blades, while providing a deep understanding of the cooling performance degradation by revealing the particle trajectories in complex vortices and the deposition characteristics of different-sized particles.
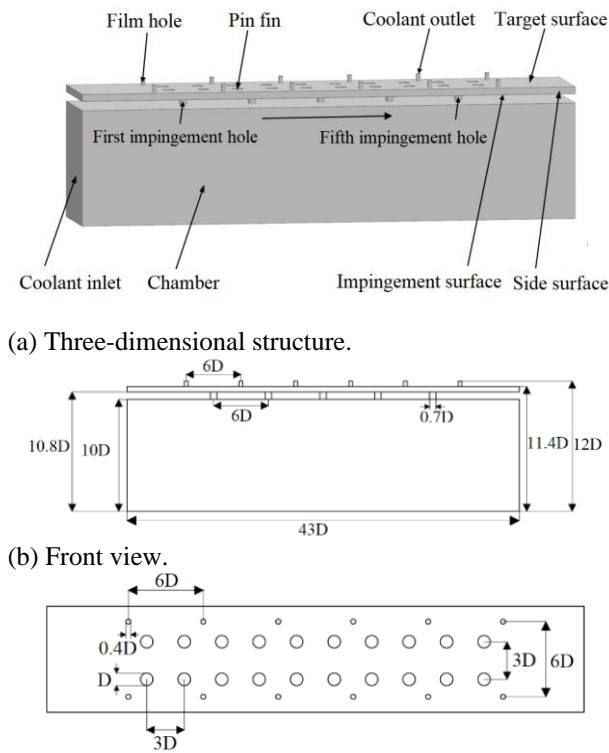
(a) Three-dimensional structure.

(b) Front view.

(c) Top view.

Fig. 1. Computational domain and geometric parameters.

Table 1 Mesh parameters

| The first layer grid size near the surface(mm)	0.01
Grid growth rate	1.2

2. NUMERICAL METHOD

2.1 Computational Domain and Mesh Generation

Figure 1 (a) shows the established computational domain consisting of the coolant chamber, 5 impingement holes, 12 film holes, and a pin fin sandwich formed by the impingement surface and target surface. The 8 film holes in the middle were shared by 5 impingement holes. The diameter of the pin fin is D=1mm and the other sizes are provided referring to the diameter of pin fin.

The geometric model was divided into the hexahedral structure grid by ICEM CFD. Mesh parameters are shown in Table 1. The results of the grid independence test using the Nusselt number on the target surface is shown in Fig. 2. (a). The change rate of the laterally averaged Nusselt number is less than 2% as the number of grids increases to exceed 20 million. Therefore, the 20 million grid was used to predict the heat-transfer character on the target surface during deposition. The local grid is shown in Fig. 2 (b). Please refer to Section 2.4 for the detailed expression of the laterally averaged Nusselt number.

2.2 Control Equations of the Fluid and Turbulence Model

The dynamic viscosity of an ideal compressible fluid as the working medium was calculated using the
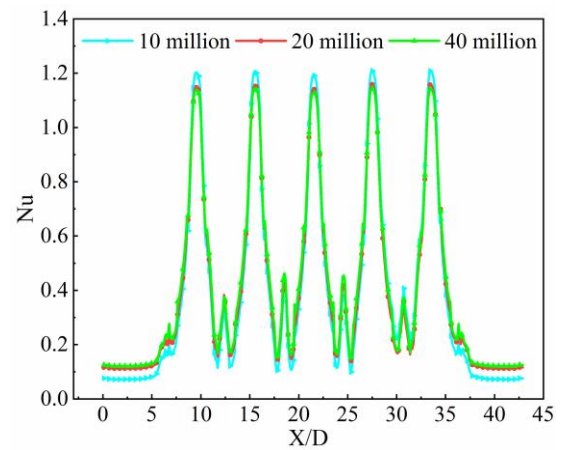
(a) Grid independence verification.
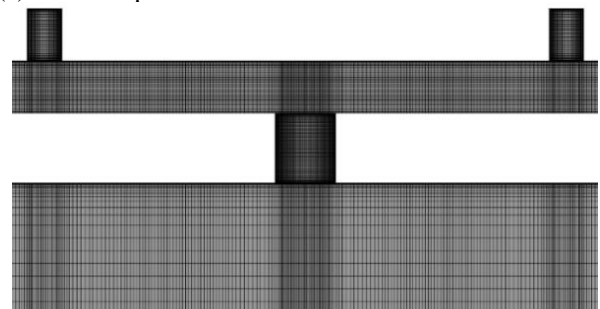
(b) Local grid.

Fig. 2. Local grid and grid independence verification.

Sutherland formula. The effect of the temperature on the specific heat and thermal conductivity were calculated using a polynomial equation. The shear stress transport (SST) K-ω turbulence model was used to predict the flow field in the viscous sublayer. The SIMPLE coupling algorithm and the second-order upwind scheme were used to discretize the items in the momentum equation and energy equation.

The migration of the particles ingested into the engine was characterized by the fluid-solid two-phase flow. Fluid and particles were respectively regarded as the continuous phase and discrete phase. The migration locus of the sand ash was described by the Lagrange method. A customized program was developed to predict the impact, adhesion, removal, and sedimentation of particles arriving at the wall surface based on the revised El-Batsh deposition model. Please refer to Section 2.3 for the detailed calculation of the revised model.

2.3 Migration and Deposition Model

The particles are subject to the drag force (F_d) generated by the relative movement of the particles and the fluid, Saffman' s lift force (F_s) generated by the strong velocity gradient, and the thermophoretic force (F_t) generated by the temperature gradient during migration. The particle migration equation is expressed as:

$$m_p \frac{du_p}{dt_p} = F_d + F_s + F_t \tag{1}$$

If the particles have a uniform temperature, the convective heat transfer equation between the fluid and the particles is:
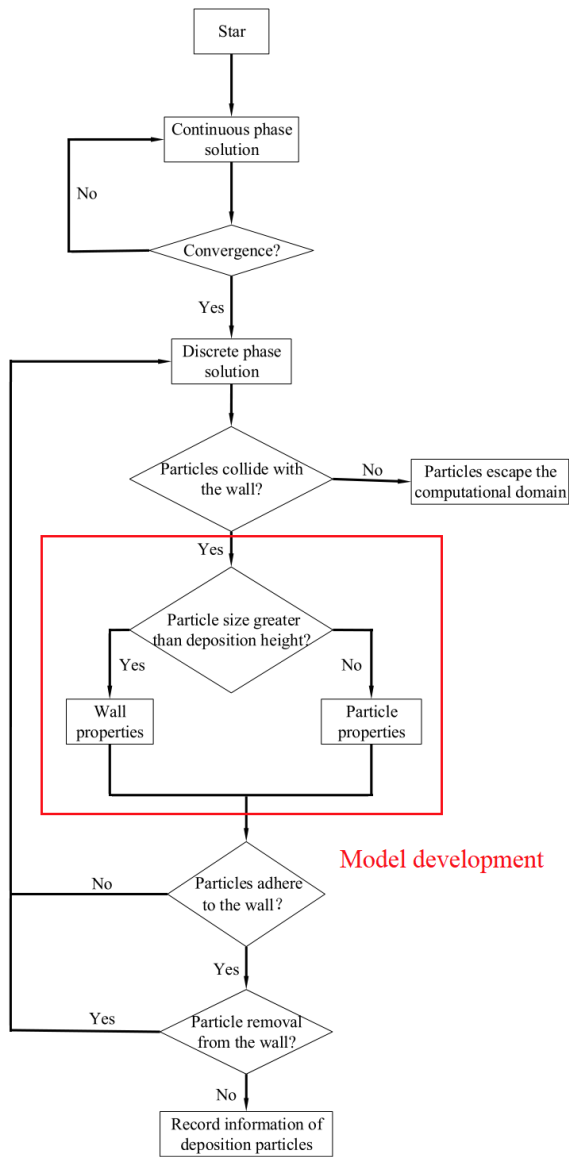
Fig. 3. Execution of the deposition model.

Table 2 Geometry and mesh parameters.

Mass flow rate of coolant into the chamber(kg/s)	8.47×10^{-5}
Coolant inlet temperature(K)	800
Target surface temperature(K)	1200
Impingement surface temperature(K)	1000
pin fin temperature(K)	1100
Side surface temperature(K)	1100
film hole outlet	Pressure outlet

Table 3 Particle information

The temperature (K) and velocity (m/s) of the injected particles	Consistent with inlet coolant
Diameter(μm)	0.2~5
Density(kg/m^3)	1700
Specific heat(J/(kg·K))	984
thermal conductivity(W/(m·K))	0.5
Volume fraction	2.87×10^{-10}

deposition model is shown in Fig 3. The Vτc also decreased with an augment in the particle diameter and Young's modulus.

Since Young's modulus affects the magnitude of the Vcr and the Vτc, we improved the method to calculate Young's modulus of the sedimentation surface because it depends on the wall properties in the initial deposition stage and the particle properties when the local deposition height is larger than the particle size. Thus, Young's modulus of the deposit surface was revised by considering the wall properties in the initial deposition stage and the particle properties when the local deposition height was larger than the particle size. The revised model considers the influence of sedimentary surface properties on deposition through wall properties and particle properties, which can predict the sedimentary characteristics of particles more accurately. By establishing a deposition model to reveal the particle trajectories in complex vortices and the deposition characteristics of different-sized particles, the degradation of cooling performance can be deeply understood.

2.4 Boundary Conditions

The boundary conditions represent typical conditions of engine turbine components. The specific parameters are shown in Table 2.

The particles were injected through the coolant inlet and are monodisperse. The particle volume fraction was much less than 10% and satisfying the conditions of the discrete model. One-way coupling existed between the flow field and the particles. The information of injected particles is shown in Table 3.

Table 4 shows the definitions of different parameters.

Where n_i, n_s, n_d, and n_e represent the numbers of colliding particles, adhering particles, deposited particles, and escaping particles, respectively. The sum of the

$$m_p c_{p,p} \frac{dT_p}{dt_p} = h_p A_p \left(T_f - T_p \right) \tag{2}$$

An empirical formula was used to decide the heat transfer coefficient of the particle surface (Ranz & Marshall, 1952a, b).

According to the El-Batsh model (El-Batsh & Haselbacher, 2002; Ai & Murray, 2012), the Vcr, which was used to determine whether the particles rebounded or adhered to the wall. If the particle velocity was exceeded the Vcr, the particle rebounded after hitting the wall. The particle rebound velocity was determined by the normal and tangential recovery coefficients obtained from Tabakoff et al. (1996). Adhesion occurred when the Vcr of the particles was exceeded the collision velocity. However, removal models were used to confirm whether the particles were deposited. If the local shear velocity was less than the Vτc, the particle was deposited. Otherwise, the particle was removed. The execution process of the

Table 4 Parameter definition

Variable	Formula
Laterally averaged Nusselt number	$Nu = \dfrac{1}{n}\sum\limits_{i=1}^{n}\dfrac{h_{fi}d_I}{\lambda}$
Collision rate	$\eta_i = n_i / n_I$
Adhesion rate	$\eta_s = n_s / n_I$
Deposition rate	$\eta_d = n_d / n_I$
Escape rate	$\eta_e = n_e / n_I$
Collision frequency	$r_i = t_i / n_i$
Number of particle collisions	$t_i = \sum\limits_{j=1}^{n_i} j \times n_1$
Adhesion probability	$p_s = t_s / t_i$
Rebound probability	$p_b = t_b / t_i$
Deposition probability	$p_d = t_d / t_s$
Removal probability	$p_e = t_e / t_s$
Collision quantity per unit area	$n_{p,i} = t_i / A_c$
Adhesion quantity per unit area	$n_{p,s} = t_s / A_c$
Deposition quantity per unit area	$n_{p,d} = t_d / A_c$
Stokes number	$St = \dfrac{\tau_p}{\tau_s} = \dfrac{\dfrac{\rho_p d_p^2}{18\mu}}{\dfrac{L_s}{V_s}}$

deposition rate and escape rate is 100%. The sum of the rebound probability and adhesion probability is 100%. The sum of the removal probability and deposition probability is 1. The Stokes number can be used to evaluate the capacity of the particles to follow the fluid flow. The particle motion is similar to the fluid flow of the fluid phase at St<<1. The particle motion is independent of the fluid phase at St>1. The particle Stokes number ranges from 0.018 to 11.21.

3. RESULTS AND DISCUSSION

3.1 Validation of Turbulence Model and Deposition Model

A row of impingement holes in the jet array was selected to establish a geometric model (Xing et al., 2010). The Nusselt number calculated by the SST K -ω turbulence model was in good agreement with the experimental results, as shown in Fig. 4(a), indicating that the SST K -ω turbulence model was suitable for calculating the jet impingement. The proposed deposition model was verified using the operating condition used by Ai and Fletcher (2012). The particle sizes in the experiments and simulations ranged from 1 μm to 20 μm with an average size of 13.5 μm. The deposition rate predicted by the proposed deposition model has a better agreement with the experimental results than with the basic deposition model, as shown in Fig. 4(b).
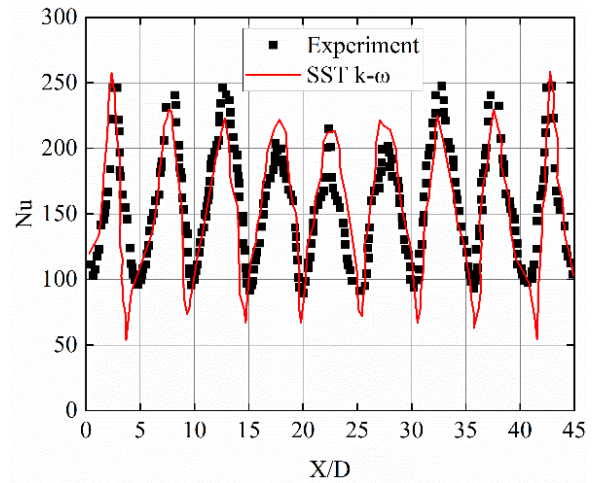
(a) Comparison of the Nu number obtained from the calculation and experiment.
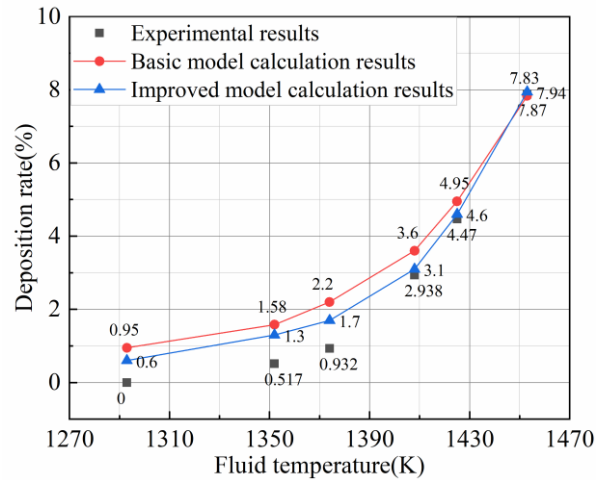
(b) Comparison of the deposition rate obtained from the calculation and experiment.

Fig. 4. Verification of deposition model and turbulence model.

3.2 Migration Characteristics of Particles with Different Diameters

The flow field in the pin fin sandwich space was characterized by the stagnation flow and the subsequent wall jet flow, as shown in Fig. 5. Stagnation flow resulted in the significant deposition in the stagnation region. The large velocity gradient and strong temperature gradient in the surface of the wall jet significantly influenced the particle forces, affecting their migration trajectories when the particles rebounded after colliding with the wall surface. Fig. 6 shows the Vcr and Vτc versus the particle diameter. The two velocities decreased rapidly with an increase in the diameter from 0.2 μm to 1.0 μm and decreased slightly when the diameter was larger than 1.0.

The velocity magnitude differed for different-sized particles, as shown in Fig. 7. The locus of the granules with diameters of 0.2 μm extended to the outlet of the film holes (Fig. 7 (a)). Some particles moved along the pin fin, indicating they were carried by the stagnation flow and subsequent wall jet flow and did not collide with the wall due to their very small Stokes number. Fig. 7(b) shows that none of the granules with diameter of 0.7 μm contacted the
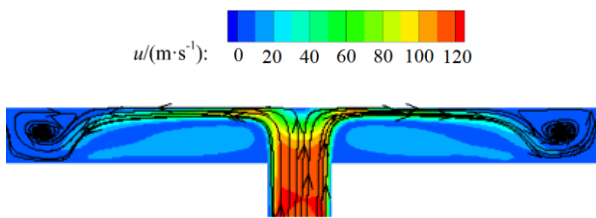
Fig. 5. Flow field in the cross-section of the center axis of the impingement holes.
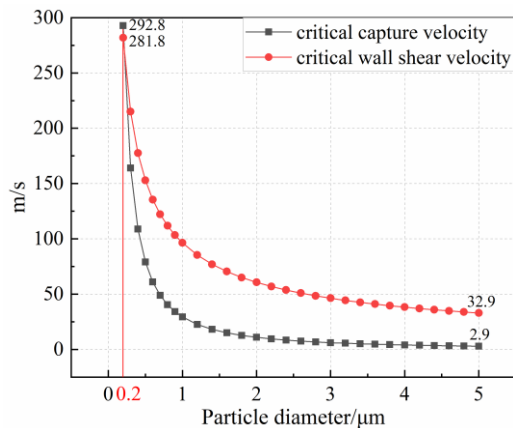

Fig. 6. The Vcr and Vτc versus the particle diameter.

wall. The particles did not follow the wall jet flow due to the larger Stokes number compared to the particles with a diameter of 0.2. Subsequently, all particles were deposited in the stagnation region due to the high critical capture velocity and low wall shear velocity. These results indicate that all particles larger than 0.7 μm in diameter collided with the wall. The low critical capture velocity caused granules with a diameter of 1.0 μm to rebound (Fig. 6 and Fig. 7(c)). The particles did not collide with the target surface and escaped from the film hole because the thermophoretic force and Saffman's lift force were larger in the outer normal direction than the drag force in the inner normal direction. Therefore, particles larger than 1.0 μm in diameter rebounded after the first collision.

All granules with a diameter of 2.0 μm immediately collided with the wall surface after they rebounded and were deposited, as shown in Fig. 7 (d). The large drag force in the inner normal direction resulted in a smaller magnitude of the secondary collision velocity than the Vcr; thus, the particles adhered to the surface. Since the adhesion position was close to the stagnation region, the granules were sediment on the wall. The position of the second collision was farther away from the stagnation point for granules with a diameter of 3.0 μm compared to those with a diameter of 2.0 μm (Fig. 7(e)). This result suggests an increased difficulty in particle deposition after the second collision. Some of the trajectories ended, and others extended to the film hole outlet after the second collision, indicating a change in the locus during the migration. Granules with a diameter of 5.0 μm exhibited multiple collisions (Fig. 7 (f)) because the larger particle diameter resulted in a smaller Vτc, and the granules were easily removed from the wall after adhesion.
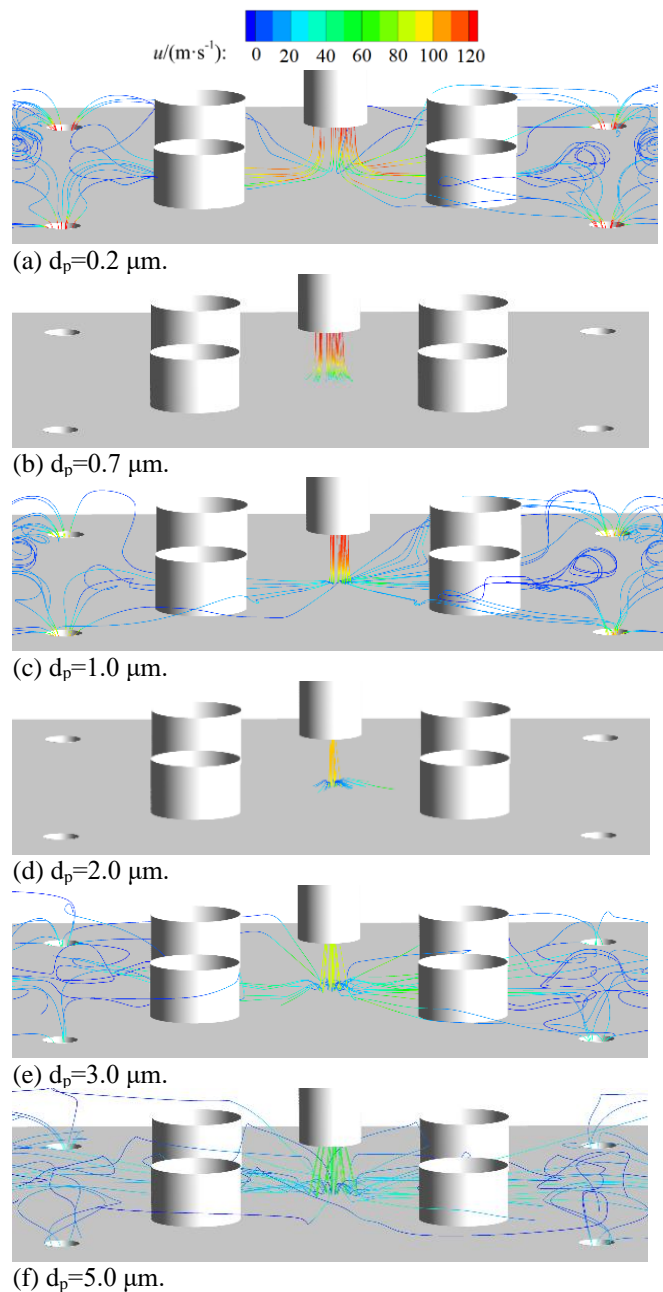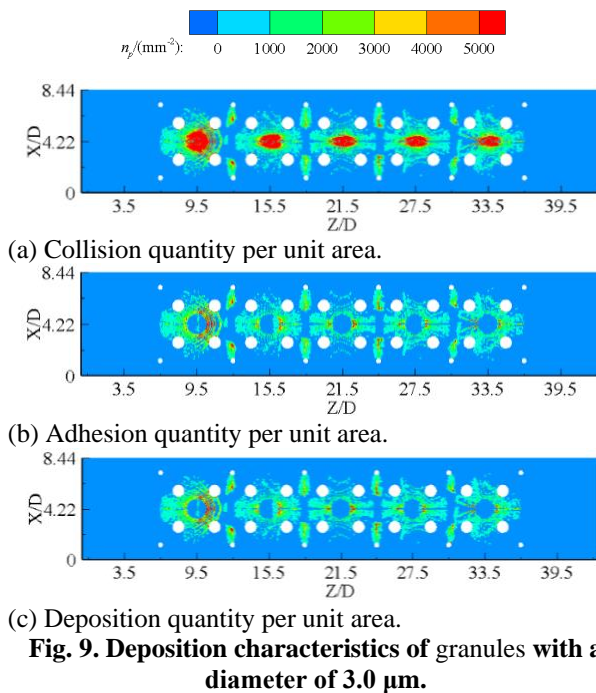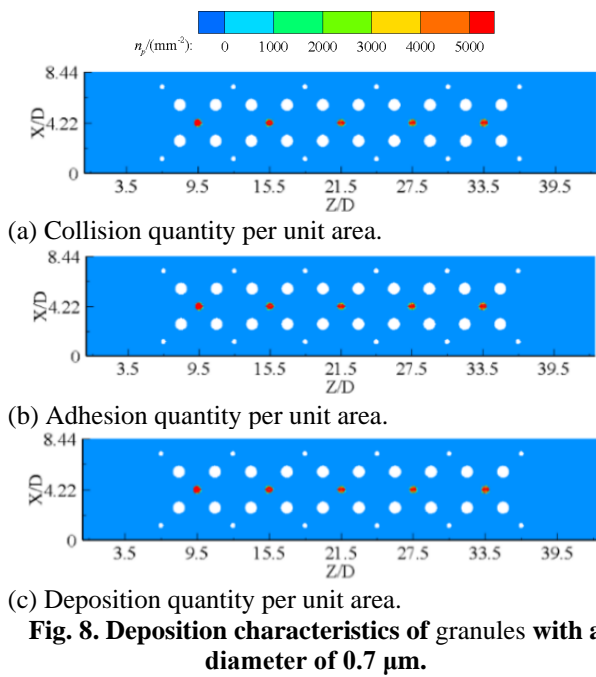

(a) d_P=0.2 μm.

(b) d_P=0.7 μm.

(c) d_P=1.0 μm.

(d) d_P=2.0 μm.

(e) d_P=3.0 μm.

(f) d_P=5.0 μm.

Fig. 7. Migration locus of particles with different diameters.

3.3 Deposition Characteristics of Different-sized Particles

Three particle sizes were selected to analyze the deposition characteristics on the target surface, as shown in Figs. 8-10. Granules with a diameter of 0.7 μm were deposited on the target surface after the first collision.

Thus, the collision, adhesion, and deposition quantities were similar (Fig. 8). Most particles were deposited around the stagnation point in an area 0.35 times the pin fin diameter. Since all granules with a diameter of 3.0 μm exiting from the impingement hole collided with the wall surface, many particles collided in the stagnation region opposite to the impingement hole, as shown in Fig. 9 (a). However, the adhesion and deposition quantities are close to zero in this region due to the rebound of all particles after the first collision. Large adhesion and deposition

(a) Collision quantity per unit area.

(b) Adhesion quantity per unit area.

(c) Deposition quantity per unit area.

Fig. 8. Deposition characteristics of granules **with a diameter of 0.7 μm.**

(a) Collision quantity per unit area.

(b) Adhesion quantity per unit area.

(c) Deposition quantity per unit area.

Fig. 9. Deposition characteristics of granules **with a diameter of 3.0 μm.**

(a) Collision quantity per unit area.

(b) Adhesion quantity per unit area.

(c) Deposition quantity per unit area.

Fig. 10. Deposition characteristics of granules **with a diameter of 5.0 μm.**

Fig. 11. Collision rate, adhesion rate, and deposition rate versus particle diameter.

quantities occurred in the area between the two pin fins in the X-direction and near the film hole in the X-direction (Fig. 9 (b) and (c)). This result implies that particles with the same diameter were deposited in different locations during migration. The collision quantity also approaches zero in the region between two adjacent cooling units. Granules with a diameter of 5.0 μm primarily adhered to and were deposited in the region enclosed by the adjacent four pin fins and two film holes, with peaks in the adhesion and deposition numbers, as shown in Fig. 10(b) and (c). The reason is that the critical capture velocity is lower for a larger particle diameter, causing the particles to migrate to the region enclosed by the adjacent four pin fins and two film holes after multiple collisions with the target surface. The maximum number of adhered particles
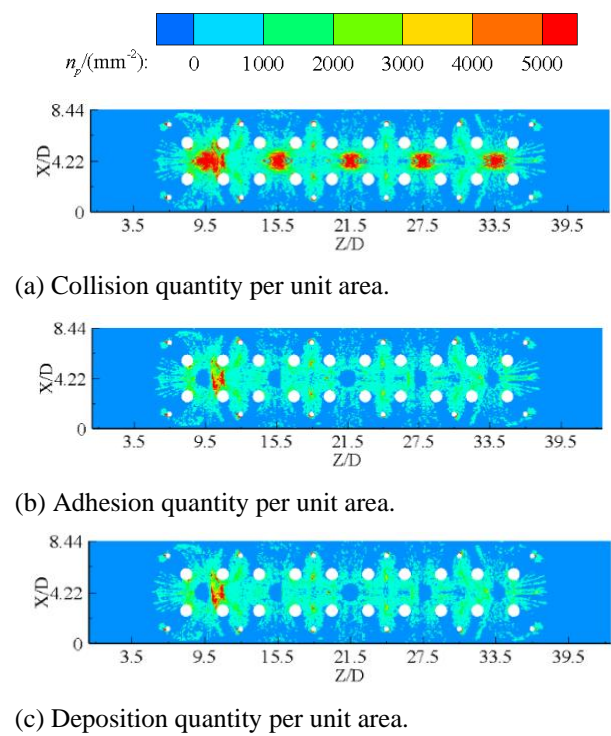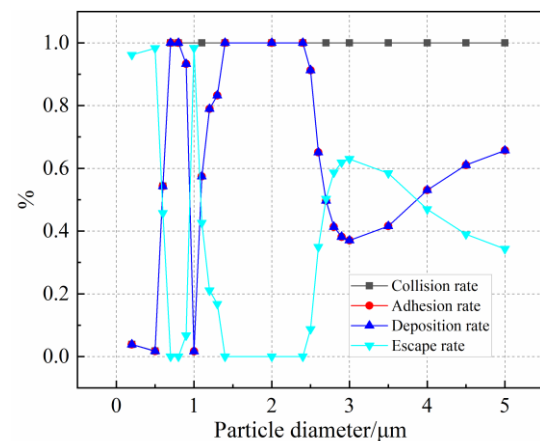
occurred in the area between the two pin fins in the X-direction. The deposition quantity around the film hole was lower than the adhesion quantity for granules with a diameter of 5.0 μm, and many particles were removed. The reason is that the Vτc is lower for a larger particle diameter. The shear velocity near the film hole was exceeded the Vτc, and the particles were removed after they adhered to this region. The adhesion and deposition quantities were high for granules with a diameter of 5.0 μm in the fountain region.

Figure 11 shows the collision rate, adhesion rate, and deposition rate for different particle diameters. Particles with a diameter range of 0.2 to 0.5 μm had a collision rate close to zero, indicating they did not collide with the wall surface and escaped from the film hole outlet during migration. Since the Stokes number of the granules in this
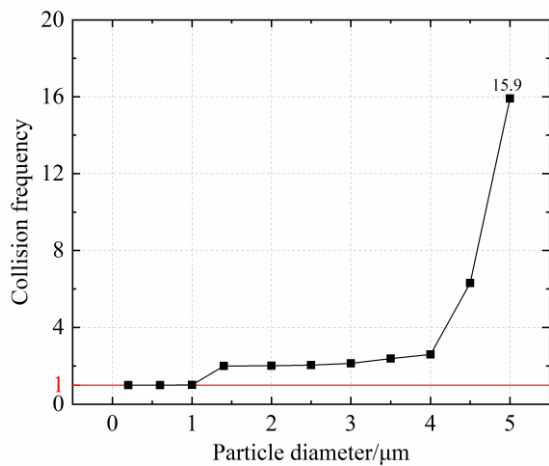
Fig. 12. Collision frequency versus particle diameter.

Fig. 13. Adhesion, rebound, deposition, and removal probabilities versus particle diameter.

Fig. 14. Overall deposition rate and deposition rates on different surfaces.

size range was much lower than 1, the inertia of the granules was low, and the followed the flow. When the granule diameter ranged from 0.5 μm to 0.7 μm, the collision rate quickly increased to 100%. The value remained at 100% as the particle diameter increased to more than 0.7μm, indicating that all particles collided with the wall, which was consistent with the previous results. The adhesion rate of the particles with diameters from 0.2 to 0.8 μm was equal to the collision rate. The reason is that the collision frequency of the particles is 1, and the adhesion probability is close to 100%, as shown in Fig. 12 and 13. These results suggest that particles adhered to the wall after the first collision because the Vcr was exceeded the normal collision velocity. The drag force and Saffman' lift force decreased, and the particle inertia increased with the particle diameter. The energy loss during the collision between the particles and the wall increased, accelerating the particle deposition on the wall.

The adhesion rate of the particles declined from 100% to nearly 0 as the diameter increased from 0.8 μm to 1.0 μm. Although the collision frequency in this diameter range was 1, the adhesion probability dropped sharply to 0. This finding indicates that particle rebound became significant after the first collision of granules with diameters from 0.8 to 1.0 μm. The adhesion rate quickly increased from 0 to 100% as the diameter increased from 1.0 to 1.4 μm. The collision frequency ranged from 1 to 2 (Fig. 12), and the adhesion probability ranged from 0 to 50% (Fig. 13), indicating that some particles adhered to the wall after the second collision.

Granules with diameters ranging from 1.4 to 2.4 μm had an adhesion rate of 100%, a collision frequency of 2.0, and an adhesion probability of 50% (Fig. 11 to 13), suggesting that all particles rebounded after the first collision and adhered to the wall after the second collision. As the number of collisions with the wall increased, the energy loss of the particles rose, increasing the probability of granule sedimentation on the wall. The lower adhesion rate and the collision frequency of 2 of granules with diameters ranging from 2.4 to 3.0 μm showed that some of the particles escaped from the film hole after the second collision. The higher adhesion rate and collision frequency indicate that some granules with diameters ranging from 3.0 to 4.0 μm adhered to the wall after multiple collisions.
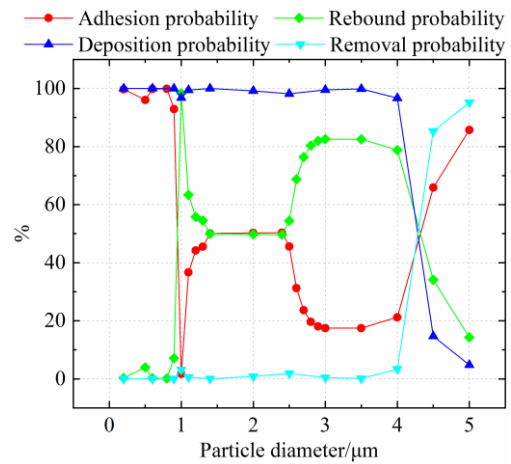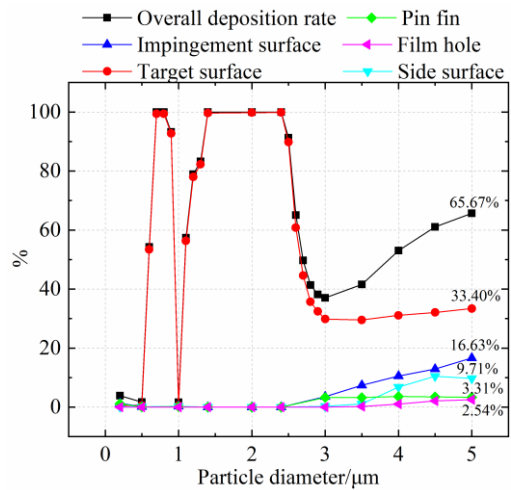
Although the adhesion rate increased as the diameter increased from 4.0 to 5.0 μm, the sharp increase in the collision frequency and adhesion probability and a substantial decrease in the deposition probability indicate that significant removal occurred. Deposition of some particles occurred after reaching the low shear velocity region during multiple removal-migration processes. Similar changes occurred in the deposition and adhesion rates as the diameter increased from 0.2 to 5 μm. The 100% deposition probability shows that deposition occurred after the granules with diameters from 0.2 to 4 μm adhered to the wall. The sum of the deposition rate and escape rate was 100%, and their curves showed opposite trends.

Figure 14 shows the deposition rates on different surfaces and the overall deposition rates for different particle diameters. When the granule diameter was less than 2.4 μm, all particles were deposited on the target surface. When the granule diameter was exceeded 2.4 μm, particle rebound and removal from the target surface was significant due to complex vortices during migration and collision. Particle deposition on the other surfaces began

on the impingement surface and pin fin surface, followed by the side surface and the film hole surface. When the particle diameter exceeded 3.0 μm, the deposition rate on all surfaces increased with an increase in the particle diameter. Since deposition on the target surface has the most significant effect on the degradation of the cooling performance, the percentage of deposition on the target surface was further analyzed. Particles with diameters of 0.7 to 0.8 μm and 1.4 to 2.4 μm were mainly sediment on the target surface. The deposition rate of granules from 2.4 to 3.0 μm on the target surface decreased rapidly, and the minimum deposition rate of particles exceeded 3.0 μm in diameter was greater than 30%, the highest deposition rate of all surfaces. The deposition rate of the other locations was very low, and the highest deposition rate was less than 20% of the deposition rate on the impingement surface. This result shows that the particles entering the impingement-effusion structure were primarily deposited on the target surface, which was the dominant reason for the degradation of the cooling performance. Therefore, reducing particle deposition on the target surface is a highly effective method for inhibiting the cooling performance degradation.

4. CONCLUSION

Complex deposition characteristics of fine particles during repeated collision, adhesion, rebound, and removal events inside an impingement-effusion structure were clarified using a deposition model. The particle deposition locations and deposition rate of different diameter particles were analyzed. The conclusions are as follows:

(1) The proposed deposition model solves the influence of sedimentary surface properties on deposition, and it can more accurately predict the deposition position and deposition rate of particles at different times than the basic deposition model. According to the particle diameter, the deposition mechanism was categorized as no deposition, deposition after the first collision, deposition after the second collision, and deposition after multiple collisions. Particles with diameters of 0.2 to 0.5 μm rarely collided with the wall and were not deposited. Most particles with diameters of 0.5 to 1.0 μm were deposited after the first collision. Deposition mechanism can be summarized that the small particles have the large critical capture velocity, so the particles easily deposit after collision with the wall. Some particles with diameters of 1.0 to 1.4 μm and 2.4 to 3.0 μm were deposited after the second collision. All particles with diameters of 1.4 to 2.4 μm were deposited after the second collision. Deposition mechanism is summarized that the phenomenon of rebound occurs due to the particle normal velocity of the first collision with wall greater than the critical capture velocity. However, the decreased normal velocity after rebound is easy to be smaller than the critical capture velocity in the second collision. Some particles with diameters exceeded 3.0 μm were deposited after multiple collisions. Deposition mechanism is summarized that larger particles have smaller critical wall shear velocity, so the wall shear velocity is more likely to be greater than the critical wall shear velocity. In the process of multiple removal-migration-adhesion, the particles can reach the

region with smaller wall shear velocity and thus deposition occurs.

(2) All particles with diameters of 0.7 to 0.8 μm and 1.4 to 2.4 μm were sediment on the target surface. When the granule diameter exceeded 2.4 μm, the granules were sediment on the other surface. At least 30% of particles with diameters exceeded 3.0 μm were deposited on the target surface. Deposition in the stagnation region occurred after the first or second collision. The deposition region enclosed by the adjacent pin fin and the film hole was observed after multiple collisions. The particles entering the impingement-effusion structure were primarily deposited on the target surface, which was the most important reason for the degradation of the cooling performance.

CONFLICT OF INTEREST

The authors declare that they have no competing interests.

AUTHORS CONTRIBUTION

W. Zhang: Conceptualization (supporting); writing; review and editing. P. Zhang: Data collection; Visualization; Writing the original draft. Y. D. Wang: Conceptualization; Data collection; Writing original draft (Supporting).

REFERENCES

Ai, W., & Fletcher, T. H. (2012). Computational analysis of conjugate heat transfer and particulate deposition on a high pressure turbine vane. *Journal of Turbomachinery*, 134(4), 1-12. https://doi.org/10.1115/1.4003716

Ai, W., Murray, N., Fletcher, T. H., Harding, S., Lewis, S., & Bons, J. P. (2012). Deposition near film cooling holes on a high pressure turbine vane. *Journal of Turbomachinery*, 134(4), 1-11. https://doi.org/10.1115/1.4003672

Bonilla, C., Clum, C., Lawrence, M., Casaday, B., & Bons, J. P. (2013, June). *The effect of film cooling on nozzle guide vane deposition*. Proceedings of ASME Turbo Expo, Texas, US.

Bons, J. P., Wammack, J. E., Crosby, J., Fletcher, D., & Fletcher, T. H. (2008). Evolution of surface deposits on a high-pressure turbine blade—part II: convective heat transfer. *Journal of Turbomachinery*, 130(2), 184–490.

Bons, J. P., Prenter, R., & Whitaker, S. (2017). A simple physics-based model for particle rebound and deposition in turbomachinery. *Journal of Turbomachinery*, 139(8), 081009–12. https://doi.org/10.1115/1.4035921

Boulanger, A., Patel, H., Hutchinson, J., Shong W. D., Xu, W., Ng, W., & Ekkad, S. (2016, June). *Preliminary experimental investigation of initial onset of sand deposition in the turbine section of gas turbines.* Proceedings of ASME Turbo Expo, Seoul, Republic of Korea.

Bowen, C. P., Libertowskiو N. D., Mortazavi, M., & Bons, J. P. (2019). Modeling deposition in turbine cooling passages with temperature-dependent adhesion and mesh morphing. ASME. *Journal of Engineering for Gas Turbines and Power*, 141(7), 1-12. https://doi.org/10.1115/1.4042287

Brach, R. M., & Dunn, P. F. (1992). A mathematical model of the impact and adhesion of microspheres. *Aerosol Science and Technology*, 16(1), 51–64. https://doi.org/10.1080/02786829208959537

Brun, K., Nored, M., & Kurz, R. (2012). Particle transport analysis of sand ingestion in gas turbine engines. *Journal of Engineering for Gas Turbines and Power*, 134(1), 1-8. https://doi.org/10.1115/1.4004187

Cowan, J. B., Tafti, D. K., & Kohli, A. (2010 June). *Investigation of sand particle deposition and erosion within a short pin fin array*. Proceedings of the ASME Turbo Expo, Glasgow, UK. https://doi.org/10.1115/GT2010-22362

Das, S. K., Sharma, M. M., & Schechter, R. S. (1995). Adhesion and hydrodynamic removal of colloidal particles from surfaces. *Particulate Science and Technology,* 13, 227–247. https://doi.org/10.1080/02726359508906680

El-Batsh, H., & Haselbacher, H. (2002, June). *Numerical investigation of the effect of ash particle deposition on the flow field through turbine cascades.* Proceedings of ASME Turbo Expo, Amsterdam, Netherlands. https://doi.org/10.1115/GT2002-30600

Forsyth, P. (2017*). High temperature particle deposition with gas turbine applications*. [Doctoral thesis, University of Oxford]. Oxford, Britain.

Jiang, L. Y., Han, Y. H., & Patnaik, P. (2018). Characteristics of volcanic ash in a gas turbine combustor and nozzle guide vanes. *Journal of Engineering for Gas Turbines and Power*, 140(7), 1-39. https://doi.org/10.1115/1.4038523

Land, C. C., Thole, K. A., & Joe, C. (2008, June). *Considerations of a double-wall cooling design to reduce sand blockage*. Proceedings of ASME Turbo Expo, Berlin, Germany. https://doi.org/10.1115/1.3153308

Laycock, R., & Fletcher, T. H. (2015). Independent effects of surface and gas temperature on coal fly ash deposition in gas turbines at temperatures up to 1400 °C. *Journal of Engineering for Gas Turbines and Power*, 138(2), 1-8. https://doi.org/10.1115/GT2015-43575

Li, G. C., Yang, P., Zhang, W., & Mo, W. S. (2020). Degradation of the cooling performance of the double wall nozzle guide vane in an engine. *Applied Thermal Engineering*, 167, 1-28.

https://doi.org/10.1016/j.applthermaleng.2019.114765

Ranz, W. E., & Marshall, W. R. (1952a). Evaporation from drops, part I and part II. *Chemical Engineering Progress* 48, 173–180.

Ranz, W. E., & Marshall, W. R. (1952b). Evaporation from drops, part I. *Chemical Engineering Progress* 48, 141–146.

Schneider, O., Dohmen, H. J., Benra, F., & Brillert, D. (2003, June). *Investigations of dust separation in the internal cooling air system of gas turbines.* Proceedings of the ASME Turbo Expo, Georgia, Atlanta. https://doi.org/10.1115/GT2003-38293

Soltani, M., & Ahmadi, G. (1994). On particle adhesion and removal mechanisms in turbulent flows. *Journal of Adhesion Science Technology*, 8(7), 763–785. https://doi.org/10.1163/156856194X00799

Tabakoff, W., Hamed, A., & Murugan, D. M. (1996). Effect of target materials on the particle restitution characteristics for turbomachinery application. *Journal of Propulsion and Power*, 12(2), 260–266. https://doi.org/10.2514/3.24022

Tian, K., Tang, Z., Wang, J., Vujanovic, M., Zeng, M., & Wang, Q. (2021). Numerical investigations of film cooling and particle impact on the blade leading edge. *Energies*, 14, 1102(1-14). https://doi.org/10.3390/en14041102

Wammack, J. E., Crosby, J., Fletcher, D., & Fletcher, T. H. (2008). Evolution of surface deposits on a high-pressure turbine blade—part I: physical characteristics. *Journal of Turbomachinery*, 130(2), 1-8. https://doi.org/10.1115/1.2752182

Wang, Z., Yin, Y., Yang, L., Yan, L., & Luan, Y. (2021). Flow and heat transfer performance of channels with 45 degree ribs in staggered array. *Journal of Applied Fluid Mechanics*, 14(5), 1535-1546. https://doi.org/10.47176/JAFM.14.05.32251

Wylie, S., Bucknell, A., Forsyth, P., McGilvray, M., & Gillespie, D. R. H. (2017). Reduction in flow parameter resulting from volcanic ash deposition in engine representative cooling passages. ASME. *Journal of Turbomachinery* 139(3), 1-13. https://doi.org/10.1115/1.4034939

Xing, Y. F., Spring, S., & Weigand, B. (2010). Experimental and numerical investigation of heat transfer characteristics of inline and staggered arrays of impinging jets. *Journal of Heat Transfe*, 132(9), 1-11. https://doi.org/10.1115/1.4001633

Yonezawa, K., Nakai, G., Takayasu, M., Sugiyama, K., Sugita, K., Umezawa, S., & Ohmori, S. (2021). Influence of blade corrosion on aerodynamic characteristics of a gas turbine. *Energy*, 230, 1-17. https://doi.org/10.1016/j.energy.2021.120665

Zhang, W., Zeng, R., Lu, J., Liu, S., Cha, H. Y., & Li, G. C. (2022). Investigation of cooling performance degradation of impingement/effusion structure on pressure side of nozzle guide vane. *Case Studies in Thermal Engineering*, 33, 1-12. https://doi.org/10.1016/j.csite.2022.101991